Aerodynamic Forces on an Airdrop Platform

Kenneth J. Desabrais*
US Army RDECOM, Natick Soldier Center, Natick, Massachusetts, 01760

An experimental investigation of the aerodynamic forces on a simplified scaled model of an airdrop platform was performed. The experiments were conducted in a water tunnel with a flat plate model at an aspect ratio of 0.56 over a Reynolds number range of 3.8×10^4 to 5.7×10^4. The lift and drag coefficients were measured with the plate at static angles of attack over the range –10º to 178º and with the plate undergoing dynamic pitching which was scaled from full-size platform motion. The results showed that the dynamic pitching of the plate significantly increased the lift and drag coefficients of the plate when compared against the plate at static angles of attack. The peak lift coefficient was increased by 72% and the maximum drag coefficient was increased by 350%. Although the peak lift coefficient occurred at the same angle of attack in both cases, the peak drag coefficient was delayed by ~42º with the dynamically pitching plate.

Nomenclature

A	=	aspect ratio, w / c	S	=	model planform area, $w \cdot c$
c	=	model or chord length	S_T	=	tunnel cross-sectional area
C_D	=	drag coefficient	t	=	time
C_L	=	lift coefficient	t_{model}	=	model thickness
C_{L_α}	=	lift-curve slope	U	=	freestream velocity
D	=	drag force	w	=	model width
F_x, F_y, F_z	=	measured force components			
L	=	lift force	α	=	angle of attack
q	=	dynamic pressure, $\frac{1}{2}\rho U^2$	ε_{sb}	=	solid blockage coefficient
Re_c	=	Reynolds number based on model length	ε_{wb}	=	wake blockage coefficient
R^2	=	coefficient of linear correlation	ρ	=	density
R_{ij}	=	correlation coefficient between variable i and j	ν	=	kinematic viscosity

I. Introduction

THE successful release and landing of payloads from aircraft using aerial delivery methods depends on the operation of many systems working in conjunction with one another in a complex and transient environment. Although airdrop systems have been used successfully for a long time, the aerodynamics of parachutes and the related airdrop equipment are not fully understood. Airdrop system performance is difficult to model and predict using analytical, numerical, and/or empirical methods because of the complex fluid structure interaction of the parachutes and other parts of the system. Although the aerodynamics of parachutes has been study limited research into the aerodynamics of other airdrop components has been limited. In particular, the aerodynamics of the payload or airdrop platform is a part of the airdrop systems which has not been extensively examined. Airdrop system simulations tools are being developed to aid in the prediction of performance parameters of new and fielded systems[1,2]. These tools can provide detailed fluid physics of a parachute or a dynamic simulation of the entire airdrop system from first motion in the aircraft until the payload reaches the ground, however the models used in these simulations tools for the platform aerodynamics are inadequate. The lift and drag on the platform is generally estimated from static flat plate analysis[2] which does not account for the dynamic nature of the platform motion.

The motion an airdrop platform experiences during parachute deployment is shown in Fig. 1 for a Low Velocity Airdrop Delivery System (LVADS). The LVADS method uses a modular Type V platform onto which the payload

* Research Aerospace Engineer, Airdrop/Aerial Delivery Directorate, 15 Kansas Street/AMSRD-NSC-AD-AT, Member AIAA.

This material is declared a work of the U.S. Government and is not subject to copyright protection in the United States.

is secured[3]. The platform initially begins a nearly horizontal orientation as it is extracted from the aircraft before pitching up to high angles (typically on the order of 120º or more). Subsequently the platform rotates back down to a horizontal orientation once the parachute system is fully deployed and inflated. A detailed dimensional analysis and study of the platform dynamics was previously completed on full-sized airdrop platforms[4] however limited data exists on the aerodynamics of an airdrop platform. A study of aerodynamic characteristics of rectangular shaped cargo containers was performed to aid in helicopter sling load investigations[5] however no other systematic investigation of platform aerodynamics is known. Dynamically pitching investigations of two-dimensional plates and airfoils have been performed[6-8] but have limited applicability to airdrop platforms given that an airdrop platform is a three-dimensional body with a small aspect ratio. Additionally the pitching airfoil studies typically examine small-amplitude oscillations which can clearly not be assumed based on the large pitch dynamics of an airdrop platform. A limited number of aerodynamic investigations on flat plates with low aspect ratios have been completed typically in connection with micro-aerial vehicle research[9-11]. These studies limited investigations to the aerodynamics of the plate to fixed angles of attack thus excluding any aerodynamic effects associated with the rotational dynamics of the plate.

The objective of this paper is to quantify the aerodynamic forces on an airdrop platform during deployment of the main parachutes. This was accomplished by experimentally measuring the aerodynamic forces on a simplified scaled model of an airdrop platform. The dynamic aspects of the aerodynamic forces are assessed by actively pitching the model in a prescribed motion which was based on the motion of a full-size airdrop platform during main parachute deployment and inflation. As a basis for comparison and to evaluate the significance of the dynamic motion of the platform, the aerodynamic forces of the platform at fixed or static angles of attack were examined as well.

II. Experimental Setup

The experiments were conducted in a water tunnel with a cross-sectional area of 61 cm × 61 cm and was 2.4 m long. The nominal axial freestream velocities were 20 and 30 cm/s with a turbulence intensity of <1.3%. A small vertical component of velocity is present in the freestream velocity which was ~2.5% of the nominal axial freestream velocity. The water temperature was 29.5 ± 0.5 ºC.

A schematic and photographs of the experimental setup is shown in Fig. 2. The airdrop platform was modeled as a flat plate. The dimensions of the model were 15.2 cm long, 8.6 cm wide and 0.56 cm thick which corresponds to an aspect ratio of $A = 0.56$ and a thickness ratio of $t_{model}/c = 3.6\%$. The aspect ratio corresponds to the aspect ratio of a 16 ft (4.9 m), Type V platform[3]. The model was constructed from ordinary flat glass to allow optical access through the model. All edges of the model were maintained sharp and no chamfering was applied to the leading or trailing edges. The model was centered in the two lateral dimensions and was located ~0.7 m from the entrance to the tunnel test section. The model was attached to a stainless steel, 1.0 cm diameter shaft (which stepped up to a 1.3 cm diameter shaft away from the model, see Fig. 2b). The model was attached to the shaft at the mid-point of its length (i.e. $c/2$) with the clamp shown in Fig. 2b.

The shaft was connected to a servomotor (QuickSilver Controls Inc., model# SilverMax S23-5-E3-6T) which drove the motion of the model in a predetermined, prescribed manner. An optical encoder was incorporated in the servomotor to measure the rotation angle of the shaft and thereby the angle of attack of the model. The initial angle of attack of the model (i.e. $\alpha = 0º$) was determined by orientating the sides of the model to be parallel with the water tunnel side walls. The uncertainty of the angle of attack of the model was estimated at ±0.5º. The encoder output an A/B quadrature signal which was converted using a digital converter (US Digital Corp., model# EDAC2) to an analog signal proportional to the rotation angle of the encoder and model. Two sets of experiments were conducted in this study. The angle of attack of the model was fixed at a series of values from –10º to 178º for the first set of experiments while the angle of attack was dynamically changed in the other set of experiments resulting in the model rotating about its mid-chord point.

Coupling the model support shaft and the servomotor was a 6-axis force/torque transducer (ATI Industrial Automation, model# Mini40 SI-20-1) which measured all the aerodynamic forces applied to the model. The transducer measured 3-axes of force and 3-axes of torque. The resolution of the measured force and moment components are listed in Table I.

Table I: Resolution of force and moment measurements

Component	Resolution	% full-scale reading
F_x, F_y	1.3×10^{-3} N	0.006%
F_z	2.5×10^{-3} N	0.004%

The tare of the model and support structure were accounted for in all force measurements. The fluid dynamic drag of the support shaft (with no model attached) was measured and removed from all force measurements made on the model. The output of the transducer was acquired on 6-six channels of a 16-bit data acquisition card. A calibration transformation matrix was applied to the raw voltage output of the transducer to convert them to SI force units. Two additional channels of the data acquisition system were used to sample the output of the servomotor optical encoder; one channel for the angle and the second channel for the rotation direction. Acquiring all data on a single data acquisition system ensured the force and angle measurements were synchronized and triggered at the same time. All channels were sampled at 150 Hz for the static angle experiments and at 1000 Hz for the dynamic pitching experiments.

Figure 3 shows a schematic of local coordinate system on the model, the force components measured by the transducer (F_x and F_y), and the resultant lift and drag forces (L and D). The transducer was orientated with its positive x-axis parallel to the axial dimension of the model and the y-axis was oriented normal to the model. The z-axis can be established based on the right-hand rule. This arrangement allowed for measuring the axial and normal aerodynamic forces of the model. The alignment of the transducer axes with the model axes was established by applying a fixed load to the model along the tunnel centerline and rotating the transducer until the force output of the transducer was maximized in the axial component and minimized in the normal component. Post-processing analysis of the force measurements suggests a transducer misalignment of - 1.25º which was corrected for in all post-processing calculations.

The Reynolds number, based on the model length,

$$Re_c = \frac{U \cdot c}{\nu} \tag{1}$$

was 3.77×10^4 and 5.65×10^4. The maximum geometric blockage (at $\alpha = 90º$) caused by the model was 3.5%. The dynamic pressure was corrected for solid and wake blockages. Based on methods in Barlow *et al.*[12], the solid blockage is given as

$$\varepsilon_{sb} = K_{sb} \frac{c \cdot w \cdot t_{model}}{S_T} \tag{2}$$

where $K_{sb} = 0.90$ and the wake blockage is given as

$$\varepsilon_{wb} = \frac{1}{4} c \cdot w \frac{C_{D_u}}{S_T} . \tag{3}$$

The corrected dynamic pressure is then given as

$$q = q_u \left(1 + \varepsilon_{sb} + \varepsilon_{wb}\right)^2 \tag{4}$$

where q_u is the uncorrected dynamic pressure.

III. Results and Discussion

A. Static Angle of Attack

The lift and drag were calculated from the measured axial and normal forces by

$$\begin{aligned} L &= F_y \cos\alpha - F_x \sin\alpha \\ D &= F_x \cos\alpha + F_y \sin\alpha \end{aligned} \tag{5}$$

These forces were further normalized as lift and drag coefficients defined as

$$\begin{aligned} C_L &\equiv \frac{L}{q \cdot S} \\ C_D &\equiv \frac{D}{q \cdot S} \end{aligned} \tag{6}$$

where the model planform area, $S = c \cdot w$, was used as the characteristic area and the corrected dynamic pressure was employed. Plots of the lift and drag coefficients as a function of the angle of attack are shown in Figs. 4 and 5. The

Reynolds number was 5.64×10^4 and each data point is based on the mean of 3000 individual measurements. The standard deviation of the mean for each point is ±0.1 and ±0.01 for the lift and drag coefficients, respectively. It should be observed that the curves in Figs. 4 and 5 are approximately symmetric about the point (90º, 0) for the lift and the 90º line for the drag given that the angles $90º \leq \alpha \leq 180º$ should correspond to angles $0º \leq \alpha \leq 90º$ if the model was rotated in the opposite direction. Also plotted in Figs. 4 and 5 are data from previous studies of flat plates with low-aspect ratios[9,10].

The lift-curve follows the results of Torres & Mueller[9] closely over the full range of their data on a model with an aspect-ratio of 0.5 and operating at a Reynolds number of 7.0×10^4. Flachsbart[10] presented lift-curves for two model at aspect-ratios of 0.2 and 1.0 which lie on either side of the lift-curve from the present study suggesting good agreement with past research. The Flachsbart model with an aspect ratio of 1.0 corresponds more closely with the present study than the plate with the lower aspect ratio of 0.2.

Absolute maximum lift values are achieved at $\alpha = 44º$ & 136º which also correspond well with the results from Flachsbart[10]. This behavior is significantly different from results for a two-dimensional flat plate[13] where the maximum lift occurs at an angle of attack of 7º - 10º after which the plate stalls. For a two-dimensional plate, the flow fully separates from the surface of the plate resulting in a reduction of lift on the plate. However for a plate with a low aspect ratio, a pair of tip vortices form on the outer edges of the plate resulting in regions of low pressure which maintain the increased lift over a wider range of angles of attack[9].

Examination of Fig. 4 shows three distinct regions in the lift curve which exhibit nearly linear behavior. These regions occur over the ranges of $-10º \leq \alpha \leq 43º$, $53º \leq \alpha \leq 129º$, and $140º \leq \alpha \leq 178º$ with rapid non-linear transitions between regions. The lift on the model increases linearly from –10º to ~43º at which point the lift peaks before a significant decline at higher angles of attack (and similarly for the region $140º \leq \alpha \leq 178º$). Comparable effects in the transition regions have been shown for flat plates with similar aspect ratios[10]. A linear least-squares regression fit was applied to each of the regions from which the lift-curve slope was estimated. The results of the regression fit are shown in Table II.

Table II. Lift-curve slope

α	$C_{L\alpha}$	R^2
$-10º \leq \alpha \leq 43º$	0.031	0.991
$53º \leq \alpha \leq 129º$	-0.021	0.999
$140º \leq \alpha \leq 178º$	0.033	0.995

The lift-curve slope for the first and last regions are nearly identical, which is expected given that the flow conditions are nearly the same. Torres & Mueller[9] report a value of 0.021 for lift-curve slope over the angle of attack range of $-10º \leq \alpha \leq 10º$. Limiting the regression fit to this same range in the present study results in a slope of 0.022, in good agreement with Torres & Mueller however a small kink reported by them in the lift-curve at $\alpha \approx 5º$ was not seen in the present study.

Through the middle region, the data exhibits very linear behavior (based on the strong coefficient of linear correlation, R^2). The zero lift crossing occurs at $\alpha = 93.5º$. Ideally this crossing should occur at $\alpha = 90º$ when the plate is at right angles to the freestream velocity and flow conditions, in the mean, are symmetric around the model thereby resulting in no lift. The source of this discrepancy could not be isolated conclusively. Potential sources considered included a fixed bias in the angle of attack due to a small misalignment with the freestream velocity, a misalignment of the force transducer with the axes of the model, interference effects between the support shaft and the model, and/or an effect associated with the small vertical component present in the water tunnel. It was concluded the discrepancy was most likely associated with a combination of these sources.

The drag curve in Fig. 5 shows an increase in the drag as the angle of attack increases until reaching a local maximum. The local maxima occur at $\alpha = 48º$ & 132º. These maxima occur at ~4º later than the peaks in the lift-curve. A sharp decline occurs immediately after the local maxima then the drag slowly increases to a maximum value of ~1.32 at $\alpha \approx 90º$. Whereas the drag curve tracks well in the range of $20º \leq \alpha \leq 40º$ with previous results, the trends in the drag curves show some discrepancies outside this range. The initial drag on the model at zero angle of attack is higher by ~0.15 than the values reported by others[9,10]. Similarly the maximum drag at $\alpha = 90º$ is higher by approximately the same amount. Hoerner[11] reports the drag coefficient for rectangular plates at right angles to the flow to be 1.17 – 1.18 which is the widely accepted value. The discrepancy is presumed to be associated with interference effects between the model and support shaft and the other issues outlined above.

Basic lifting line theory can be used to predict the drag on finite wings. The drag on a finite aspect ratio wing is often modeled as[14]

$$C_D = C_{D_o} + K \cdot C_L^2 \tag{7}$$

where C_{D_o} represents the drag of the wing cross-section (i.e. the unit span drag of an airfoil with same cross-section as the wing) and the second term represents the induced drag associated with finite-wings. The value of K is a function of the lift distribution on the wing and its aspect ratio where $K = 1/(\pi e \cdot A)$ and e is a function of the circulation distribution on the wing with values for $e \leq 1$. Although the underlying assumptions high Reynolds number and large aspect ratio inherent with lift line theory are not applicable to the present study, a simple relationship for predicting the drag on the plate is desired. It was decided to apply the relationship given in Eq. (7) to the present data however estimates for the two coefficients are needed. These values are estimated by plotting C_D as a function of C_L^2 (Fig. 6a) and applying a linear regression fit. The regression fit gives a slope of $K = 0.552$ ($e = 1.03$) and an intercept of $C_{D_o} = 0.140$ with a coefficient of linear correlation of $R^2 = 0.991$. Torres & Mueller[9] report $K = 0.82$ ($e = 0.78$) for a flat plate with $A = 0.5$, however their estimate is based on the angle of attack range -10º $\leq \alpha \leq$ 10º. The discrepancy existing with the present data results primarily due to the higher drag values at lower angles of attack, which tend to lower the slope value. The lack of agreement further suggests the underlying assumptions of the lifting line theory are not applicable to the present situation. However given the dearth of appropriate low Reynolds number, low–aspect ratio wing theories, and to provide a means for comparison with other studies on flat plate aerodynamics, the drag was estimated using Eq. (7). The drag of the plate is estimated by the relationship,

$$C_D = C_{D_o} + K \cdot \left[C_L(\alpha = 0) + C_{L_\alpha} \cdot \alpha \right]^2 \tag{8}$$

where $C_L(\alpha=0)$ is the lift coefficient at zero angle of attack and C_{L_α} is the lift-curve slope. Both these values are obtained from the linear regression fit applied to the lift-curve above (Table II). Using those coefficients, Eq. (8) simplifies to

$$C_D = 0.140 - 0.00090 \cdot \alpha + 0.00059 \cdot \alpha^2 \tag{9}$$

for the range 0º $\leq \alpha \leq$ 43º. The results obtained from Eq. (9) are plotted in Fig. 6b and shows strong agreement with measured experimental data.

B. Dynamic Pitching

A full-sized airdrop payload experiences large amplitude pitching and oscillations during airdrop operations. The extraction of the payload from the aircraft and the deployment of parachute systems apply significant forces and moments to the airdrop platform causing these oscillations and rotations. A dimensional analysis on the motion of a full-size airdrop platform was detailed in Desabrais[4]. A motion profile, based on this dimensional analysis and the motion of a full-size airdrop platform[15,16], was created for the scaled water tunnel model. The desired motion profile and the resultant rotational output from the servomotor is plotted in Fig. 7. The angular velocity and acceleration were estimated from the measured angle of attack by numerical differentiation using a central differencing scheme. It should be noted the angular acceleration has been digitally filtered using a 50th order window-based finite impulse response (FIR) filter with a cut-off frequency of 30 Hz in order to reduce the noise introduced by the differentiation operation. The measured output follows the desired motion with the exception of a small offset (~5º) in the angle of attack. The motion consists of a rapid pitching up of the platform which approaches a maximum angle of ~132º and then subsequently undergoes a series of oscillations of declining amplitude. The initial peak to peak amplitude of the oscillations is ~45º and is reduced to a *rms*-amplitude of ~4º (i.e. 4.0%) about a mean angle of attack of 95.6º .

The lift and drag for the model undergoing the motion given in Fig. 7 is plotted in Fig. 8. This plot is the ensemble average of 32 individual trials. The Reynolds number for these trials was 3.77×10^4. Also plotted in Fig. 8 is the angle of attack as a function of time. The lift and drag initially increase as the angle of attack increases towards its maximum level. Maximum values in the lift and drag are achieved during the angle of attack ascent, prior to the angle of attack reaching its peak value. Once the maximum angle of attack is reached, the lift and drag have declined substantially to lower values and begin to oscillate about mean values which approach those seen for the plate at an equivalent static angle (see Figs. 4 and 5). The *rms*-amplitude of the lift and drag coefficient oscillations for long times (i.e. $t \geq 8$ s) are 0.12 ($C_{L_{rms}} / C_{L_{mean}} = 126\%$) and 0.11 ($C_{D_{rms}} / C_{D_{mean}} = 8.0\%$).

The aerodynamic forces undergo a series of oscillations which are approximately 180º out of phase with the angle of attack. This is verified by calculating the correlation coefficient R_{ij} for the two parameters after the initial

pitch up of the platform is achieved (i.e. $t \geq 3$ s). A correlation coefficient has values of $-1 \leq R_{ij} \leq 1$ with a value of one showing the two signals are perfectly correlated and in-phase whereas a value of –1 corresponds to the two signals being perfectly anti-correlated (i.e. 180º out of phase). The correlation coefficient between the angle of attack and the lift and drag coefficients is –0.70 and –0.43, respectively. Both force components show a strong anti-correlation (i.e. the signals are out-of-phase) with the angle of attack. This suggests the aerodynamic forces lag the pitching motion of the platform.

The effects of the dynamic pitching of the platform can be seen by comparing the lift and drag forces with those seen for the plate at static angles of attack. Figure 9 plots the lift and drag coefficients for the dynamically pitching plate as a function of the angle of attack for $0 \text{ s} \leq t \leq 3.6$ s. Also included in the plot are the lift and drag coefficients for the plate at static angles of attack. Comparing the lift-curves, the peak lift occurs at $\alpha \approx 43º$ for both the rotating plate and the plate at static angles. However, the rotating plates achieves a peak lift value ~72% greater than the static angle value. The plate at static angles shows a rapid decline in the lift after achieving its peak value whereas the dynamically pitching plate maintains it peak value over a broader range before an appreciably decline is seen. The initial pitch-up of the plate appears to follow an approximately linear trend. Applying a linear regression fit to the initial pitch up of the platform (i.e. from the initial angle of attack until the peak value is approached, $0º \leq \alpha \leq 41.4º$), results in a lift-curve slope of 0.048, a 50% increase over the lift-curve slope for the plate at static angles of attack.

The drag exhibits similar trends as observed in the lift-curve behavior. The drag of the rotating plate shows a rapid rise which approaches a maximum value at an angle of attack delayed significantly when compared to the plate at static angles. The peak drag value occurs at $\alpha = 90.4º$ compared to 48º for the first local maximum of the plate at static angles. The rotating plate achieves a peak drag coefficient value of 4.5, a 350% increase over the plate at static angles. In addition, the drag coefficient of the rotating plate at $\alpha = 48º$ (i.e. the peak static angle drag) is twice the magnitude of the static angle drag. Whereas the plate at static angles of attack has a rapid drop-off in the drag immediately after the maximum, the drag of the rotating plate maintains significantly higher values over a broader range of angles of attack. After achieving its peak value, the drag is reduced in magnitude and begins to approach and oscillate around the drag coefficient value of a plate at ~90º (i.e. $C_D \approx 1.36$). These oscillations are seen in the forces curves in the region $70º \leq \alpha \leq 130º$.

IV. Conclusions

The aerodynamic forces on a low-aspect ratio flat plate were examined with the plate at static angles of attack and while the plate was pitched dynamically in a predetermined, prescribed manner. The plate rotation was scaled from the motion of a full-size airdrop platform during deployment and inflation of its parachute system. The experiments were conducted with a model which had an aspect ratio of 0.56 and Reynolds number range of $3.8 \times 10^4 - 5.7 \times 10^4$. The results from the plate at static angles of attack showed good comparison with previous results. The dynamic pitching of the plate resulted in a significant increase in both the lift and drag coefficients over the full range of angles of attack. The peak value of the lift coefficient for the pitching plate showed a 72% increase over the plate at static angles of attack. The peak value of the lift coefficient occurred at the same angle attack for both cases. The drag coefficient showed a more dramatic increase of 350% at an angle of attack delayed by 42º over that seen in the plate at static angles. The significant differences between the dynamically pitching plate and the plate at static angles of attack clearly shows modeling the aerodynamic forces with a low-aspect ratio flat plate at static angles of attack does not effectively capture the transient nature of the dynamics of the fluid flow. This suggests more advanced models (analytical, numerical, and empirical) are needed to predict the aerodynamic forces on the platform.

References

[1]Stein, K.R., Benney, R.J., Tezduyar, T.E., Leonard, J.W., and Accorsi, M.L., "Fluid-Structure Interactions of a Round Parachute: Modeling and Simulation Techniques," *Journal of Aircraft*, Vol. 38, No. 5, 2001, pp. 800-808.

[2]Cuthbert, P.A., "A Software Simulation of Cargo Drop Tests," Proceedings of the 17th AIAA Aerodynamic Decelerator Systems Technology Conference, May 19-22, 2003, pp. 229-239; AIAA Paper 2003-2132.

[3]FM 4-20.102/NAVSEA SS400-AB-MMO-010/TO 13c7-1-5, "Airdrop of Supplies and Equipment: Rigging Airdrop Platforms," August 22, 2001

[4]Desabrais, K.J., "The Motion and Aerodynamics of an Airdrop Platform," *22nd AIAA Applied Aerodynamics Conference*, Providence, RI, AIAA Paper 2004-4845, Aug. 2004.

[5]Laub, G.H. and Kodani, H.M., "Wind Tunnel Investigation of Aerodynamic Characteristics of Scale Models of Three Rectangular Shaped Cargo Containers," NASA TM X-62,169, July 1972.

[6]Walker, J.M., Helin, H.E., and Strickland, J.H., "An Experimental Investigation of an Airfoil Undergoing Large-Amplitude Pitching Motions," *AIAA Journal*, Vol. 23, No. 8, 1985, pp. 1141-1142.

[7]Carr, L.W., "Progress in Analysis and Prediction of Dynamic Stall," *Journal of Aircraft*, Vol. 25, No. 1, 1988, pp. 6-17.

[8]Visbal, M.R. and Shang, J.S., "Investigation of Flow Structure Around a Rapidly Pitching Airfoil," *AIAA Journal*, Vol. 27, No. 8, 1989, pp. 1044-1051.

[9]Torres, G.E. and Mueller, T.J., "Aerodynamic Characteristics of Low Aspect Ration Wings at Low Reynolds Numbers," *Fixed and Flapping Wing Aerodynamics for Micro Air Vehicle Applications*, edited by T.J. Mueller, Progress in Astronautics and Aeronautics, AIAA, Reston ,VA, 2001, pp. 115-141.

[10]Flachsbart, O. "Messungen an Eben und Gewölbten Platten," *Ergebnisse der Aerodynamischen Versuchsantalt zu Göttingen, IV. Lieferung*, edited by L. Prandtl and A. Betz, Verlag von R. Oldenbourg, Munich, 1932, pp. 96-100.

[11]Hoerner, S.F., *Fluid-Dynamic Drag*, published by author, Midland park, NJ, 1958, Chap. 3.

[12]Barlow, J.B., Rae, W.H., and Pope, A., *Low-Speed Wind Tunnel Testing*, 3rd ed., John Wiley & Sons, New York, 1999, Chap. 10.

[13]Selig, M.S., Donovan, J.F., and Fraser, D.B., *Airfoils at Low Speeds*, H.A. Stokely, Virginia Beach, Virginia, 1989, pp. 229-230.

[14]Anderson, J.D., *Fundamentals of Aerodynamics*, 3rd ed., McGraw Hill, New York, 2001.

[15]Machin, R., Stein, J., Muratore, J., "An Overview of the X-38 Prototype Crew Return Vehicle Development and Test Program," *15th CEAS/AIAA Aerodynamic Decelerator Systems Technology Conference*, Toulouse, France, AIAA Paper 99-1703, June, 1999, pp. 20-37.

[16]Cuthbert, P.A. and Desabrais, K.J., "Validation of a Cargo Airdrop Software Simulator," Proceedings of the 17th AIAA Aerodynamic Decelerator Systems Technology Conference, Monterey, CA, AIAA Paper 2003-2133, May, 2003, pp. 240-250.

Figure 1. A series of pictures showing a typical deployment of cargo during an airdrop operation.

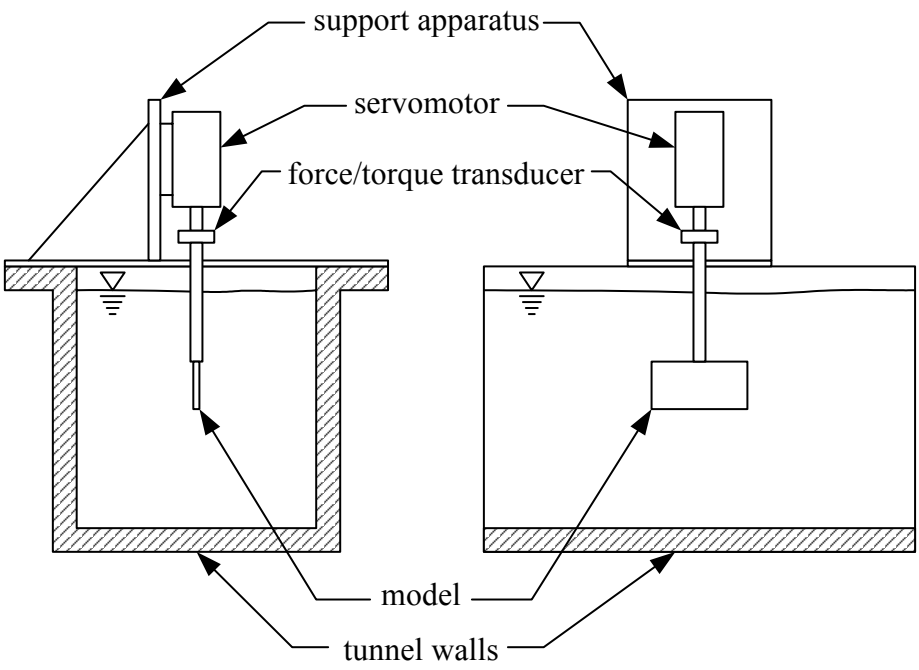

a)

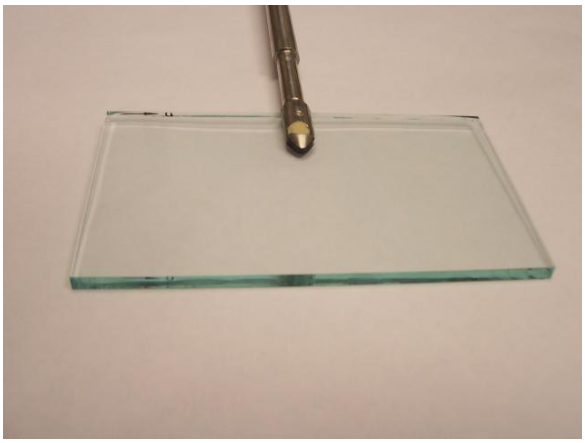

b)

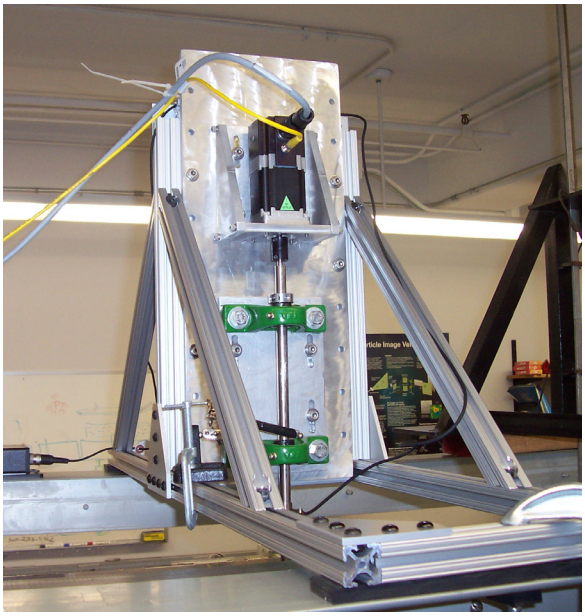

c)

Figure 2. a) Schematic of the experimental setup; b) photo of the plate, clamp and support shaft, and c) photo of the servomotor, shaft and support apparatus.

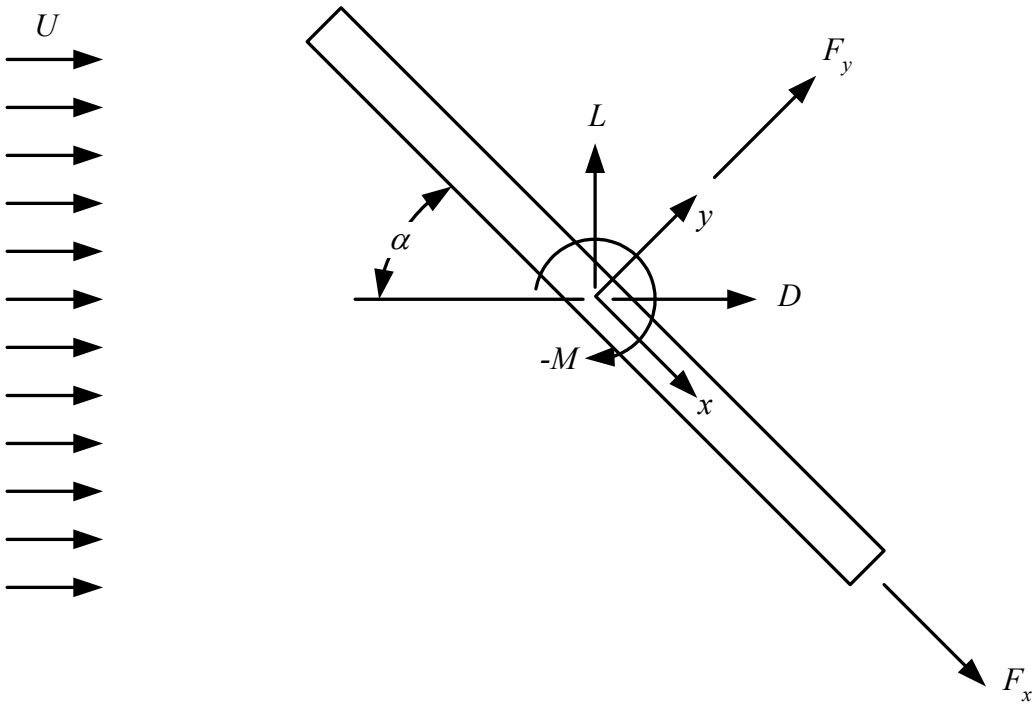

Figure 3. Diagram of the plate showing the orientation of the force transducer axes and the force components measured on the plate.

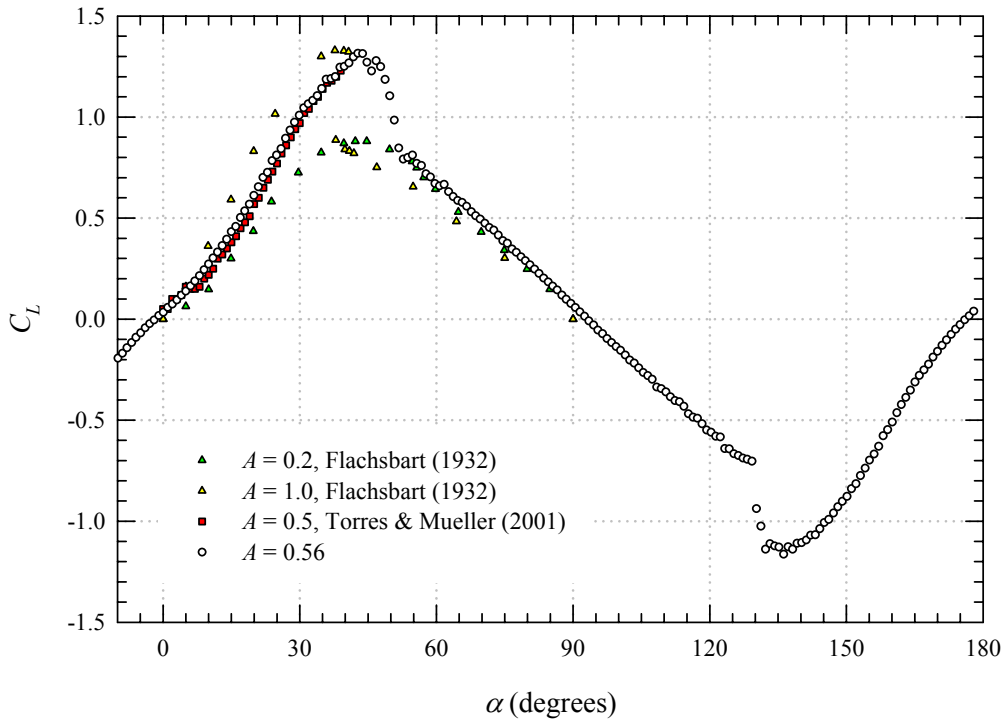

Figure 4. The lift coefficient of the plate at static angles of attack.

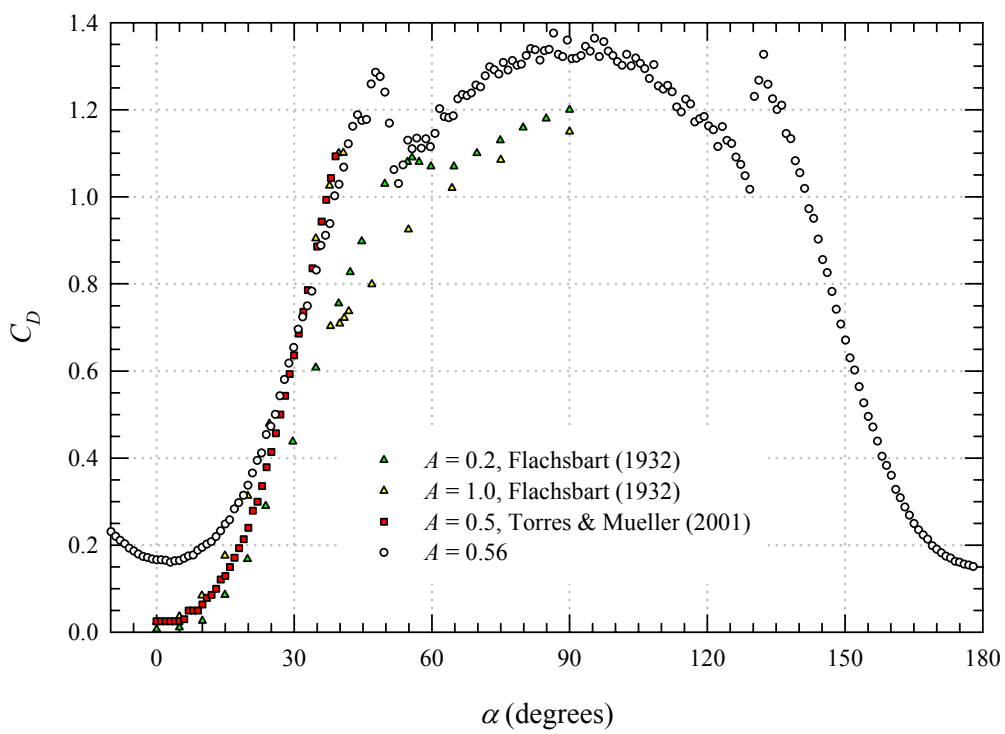

Figure 5. The drag coefficient of the plate at static angles of attack.

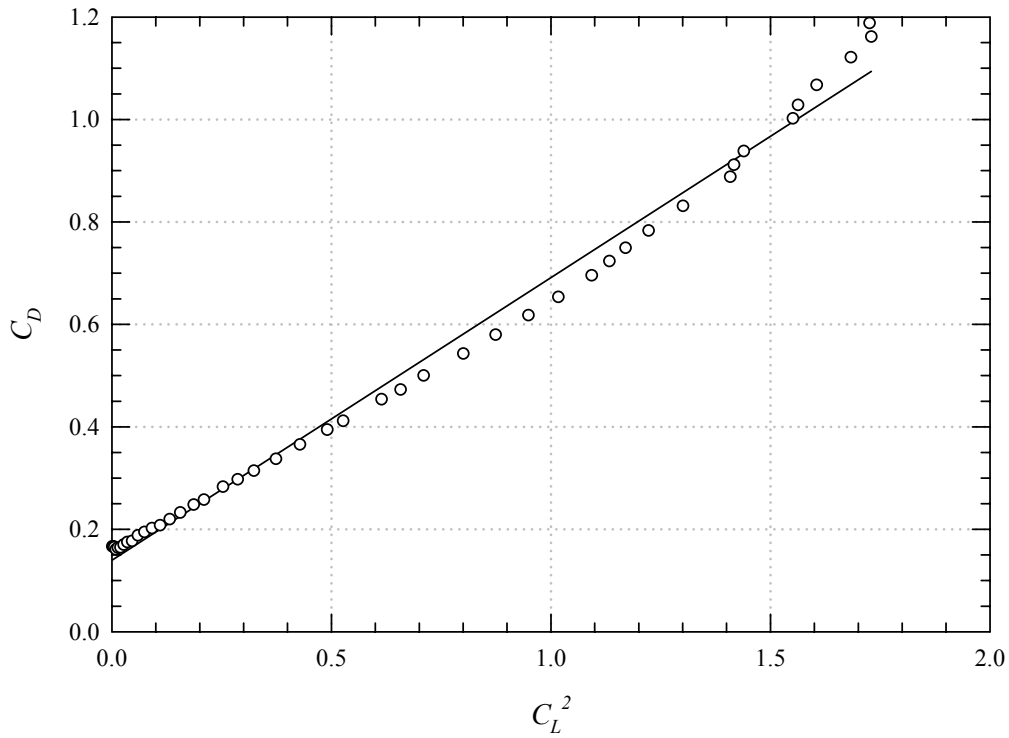

a)

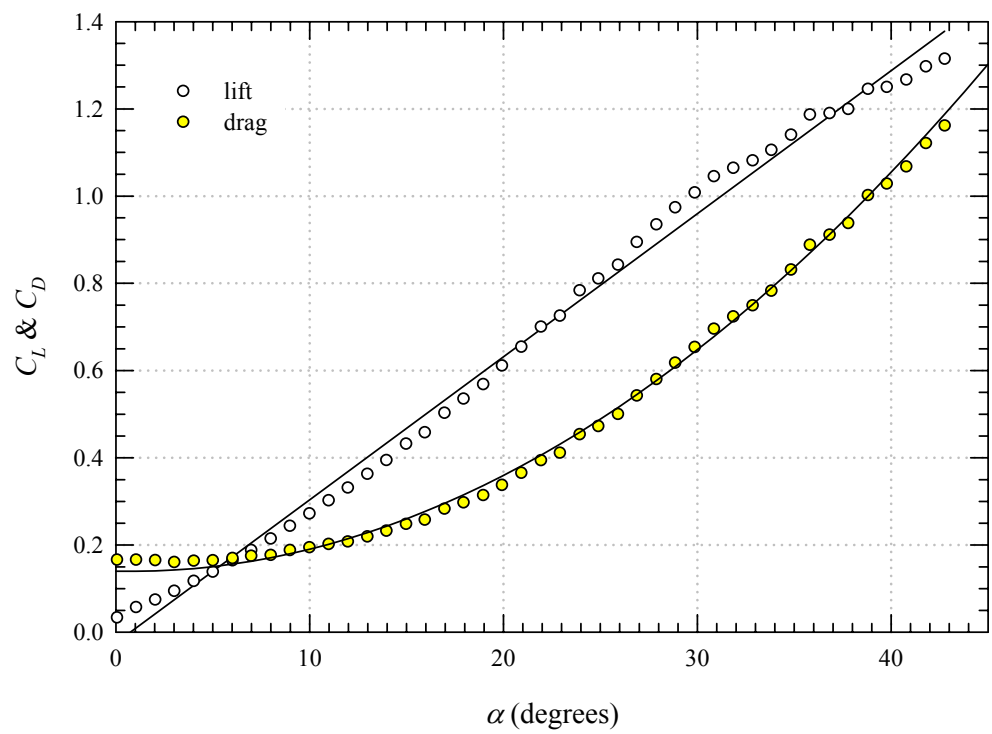

b)

Figure 6. a) Linear regression fit of drag coefficient as a function of the lift coefficient squared, b) linear regression fit of the lift coefficient and predicted drag coefficient based on a simple quadratic expression of the lift coefficient (Eq. (9)). The data points represent measured lift and drag coefficients.

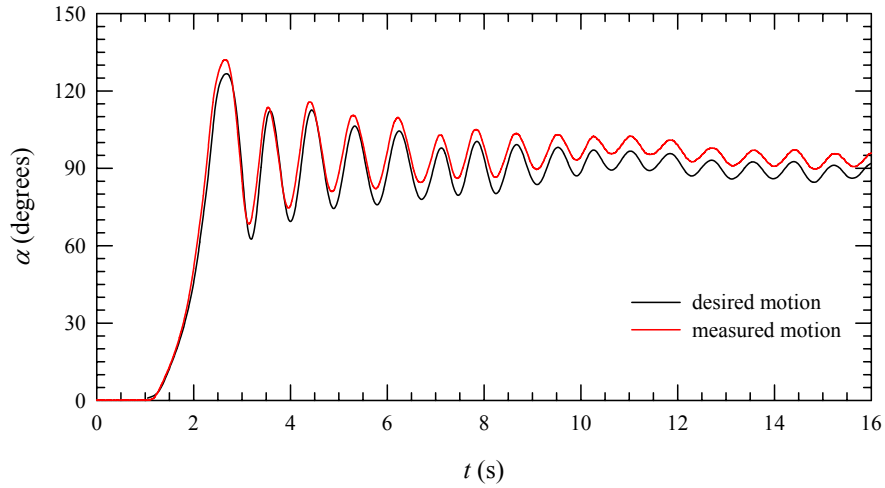

a)

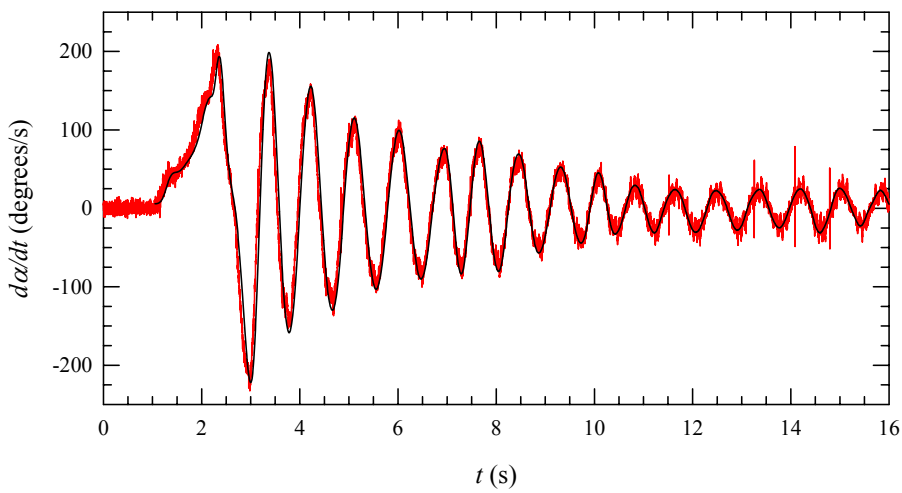

b)

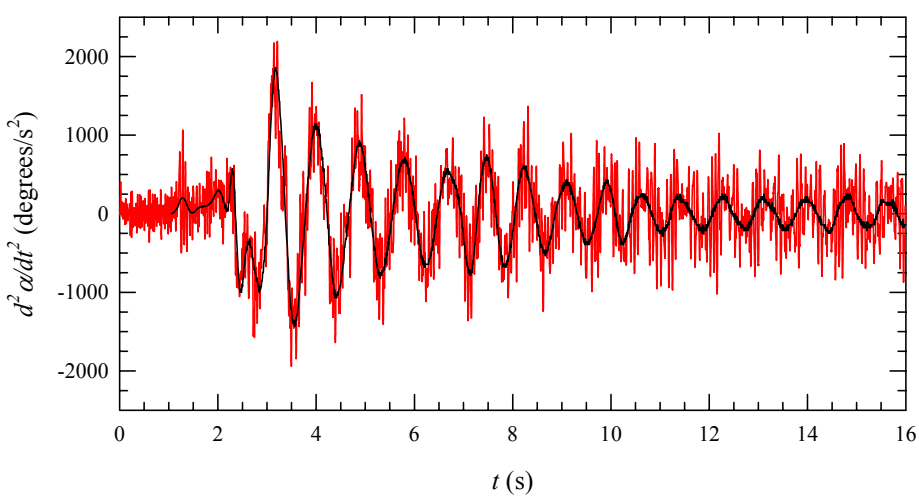

c)

Figure 7. Motion profile of the flat plate based on a full-size airdrop platform scaled to laboratory scales. a) angle of attack, b) angular velocity, and c) angular acceleration.

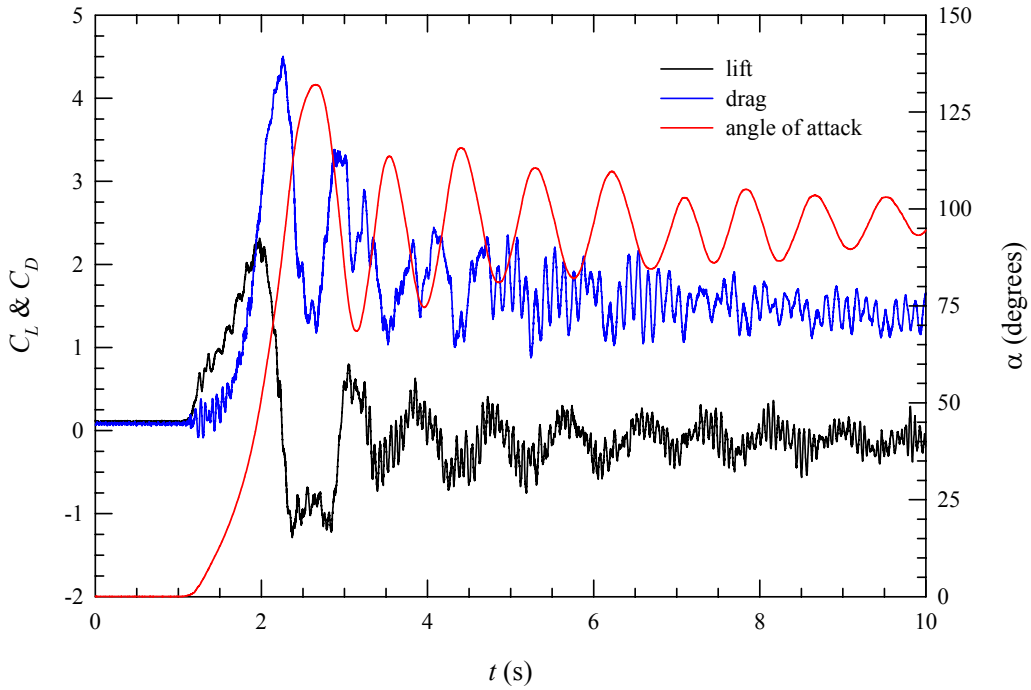

Figure 8: Lift and drag coefficients of a flat plate with an aspect ratio of 0.56 undergoing the rotation shown in Fig. 7 at a Reynolds number of 3.8×10^4.

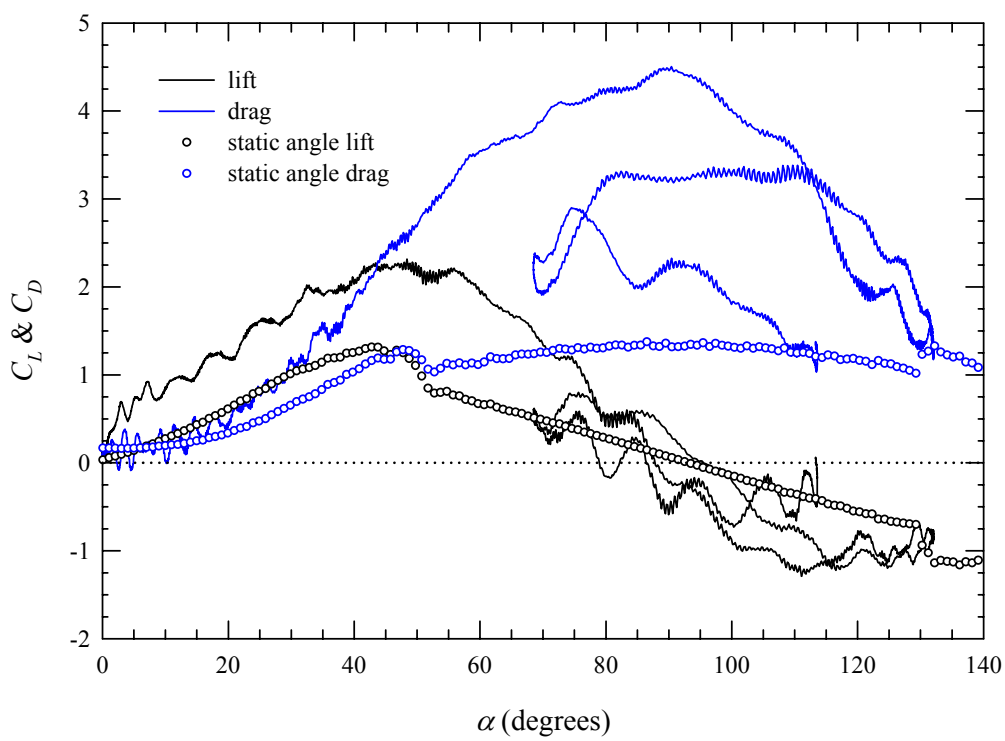

Figure 9: Lift and drag coefficient as a function of angle of attack for $t \leq 3.6$ from Fig. 8. The data points are the lift and drag coefficients from the plate at static angles, duplicated from Figs. 4 and 5.